PCCP

ROYAL SOCIETY OF CHEMISTRY

PAPER

Cite this: *Phys. Chem. Chem. Phys.*, 2018, **20**, 20970

A quantum-mechanical investigation of oxygen vacancies and copper doping in the orthorhombic $CaSnO_3$ perovskite†

Jefferson Maul, *[abc] Iêda Maria Garcia dos Santos,[b] Julio Ricardo Sambrano,[c] Silvia Casassa[a] and Alessandro Erba[a]

Received 1st June 2018,
Accepted 25th July 2018

DOI: 10.1039/c8cp03481h

rsc.li/pccp

In this study we explore the implications of oxygen vacancy formation and of copper doping in the orthorhombic $CaSnO_3$ perovskite, by means of density functional theory, focusing on energetic and electronic properties. In particular, the electronic charge distribution is analyzed by Mulliken, Hirshfeld-I, Bader and Wannier approaches. Calculations are performed at the PBE and the PBE0 level (for doping with Cu, only PBE0), with both spin-restricted and spin-unrestricted formulations; unrestricted calculations are used for spin-polarized cases and for the naturally open-shell cases (Cu doping). An oxygen vacancy is found to have the tendency to reduce Sn neighbors by giving rise to an energy band within the energy band-gap of the pristine system, close to the valence band. At variance with what happens in the $CaTiO_3$ perovskite (also investigated here), an oxygen vacancy in the $CaSnO_3$ perovskite is found to lose two valence electrons and thus to be positively charged so that no F-center is formed. Regarding Cu doping, when one Sn atom is substituted by a Cu one, the most stable configuration corresponds to having the Cu atom as a first neighbor to the vacancy. These findings shed some light on the catalytic and phosphorous host properties of this perovskite.

1 Introduction

Perovskites, and in particular those belonging to the ABO_3 family, are a class of materials characterized by a large variety of cationic and anionic compositions of great interest in solid state science because of their many possible applications.[1–8] Calcium stannate perovskite, $CaSnO_3$, has promising use as a phosphorous host,[9–13] in components of optoelectronic devices,[14] in catalysis,[15] and as an unconventional luminescent material.[16–18]

Point-defects of ordered materials represent one of the most studied topics in materials science, given that they can significantly alter physical and chemical properties. Among those, the oxygen vacancy is clearly one of the most commonly reported point-defects of oxide-based catalysts.[19–28] In particular, a wealth of information on this subject is available for the prototypical TiO_2 catalyst, in which this defect is "easily" formed in its reactive type.[29–31] Doping (*i.e.* atomic substitution) is another popular source of point-defects that, if properly controlled, can be used to tune some properties of the material.[32–37]

An oxygen vacancy V_O in an ionic material can range between two ideal limits: neutral, $V_O^{\times}$ and doubly positively-charged, $V_O^{\bullet\bullet}$, the neutral one being commonly associated with an F-center (color center) in perovskite structures.[38–40] Three previous theoretical studies addressed the issue of the formation of an oxygen vacancy in the $CaSnO_3$ perovskite. The first study was carried out by Urusov *et al.*[41] and took advantage of a classical description of an ionic lattice. The second one used a high-throughput density functional approach to screen more than 5000 perovskite structures; among them, Emery and Wolverton proposed the stability of orthorhombic $CaSnO_3$ and studied the formation of an oxygen vacancy.[42] The third used density functional theory, DFT, calculations of the vacancy concomitant to lanthanum doping of some alkaline earth stannates.[43]

In this study, we characterize the energetic and electronic aspects of the formation of an oxygen vacancy in the $CaSnO_3$ orthorhombic perovskite by using DFT in the generalized-gradient approximation (GGA) and with a hybrid approach, including some non-local exact exchange. We also focus our attention to Cu-doping given that this element is considered in

---

[a] *Dipartimento di Chimica, Università degli studi di Torino, Via Giuria 5, 10125 Torino, Italy. E-mail: jmauldea@unito.it*
[b] *Núcleo de Pesquisa e Extensão, Laboratório de Combustíveis e Materiais, Universidade Federal da Paraíba, CEP 58051-900, João Pessoa, PB, Brazil*
[c] *Computational Simulation Group, CDMF-UNESP, São Paulo State University, CEP 17033-360, Bauru, SP, Brazil*

† Electronic supplementary information (ESI) available: Mulliken and Hirshfeld charges for all calculations, centroids of the bond Wannier functions, band structure of $CaTiO_3$ and spin density 3D maps of $CaTiO_3$. See DOI: 10.1039/c8cp03481h

several studies as a tuning medium for catalytic activity, particularly so in Sn containing structures.[44–48] Formation energies are computed, the electronic structure of the defect-containing structures analyzed in terms of the projected density-of-states and the electron charge distribution of the defects investigated in terms of Mulliken, Hirshfeld-I, Bader and Wannier approaches, which, when combined, provide a rather comprehensive characterization of the defects.

2 Methodology and computational setup

All calculations are performed using the Crystal17 program.[49–51] We use all-electron atom-centered Gaussian-type-function (GTF) basis sets, the same as already used in our previous studies on this system.[52,53] They are described by 8(s)6511(sp)21(d), 9(s)763111(sp)631(d) and 6(s)2111(sp)1(d) contraction of primitive GTFs for Ca, Sn and O atoms, respectively. Additionally for Cu atoms an 8(s)64111(sp)41(d) all-electron basis set is considered.[54] The calculations are performed at the PBE[55] and the PBE0[56] level. The tolerances for the evaluation of Coulomb and exchange series are set to 7,7,7,7,14.[57] The convergence of energy was set to 10^{-8} Hartree for the optimization procedure using a quasi-Newton optimizer combined with a BFGS algorithm for Hessian updating. The shrinking factor was set to 8 for the bulk (20 atoms per cell) and to 2 for the 2 × 2 × 2 supercell (160 atoms per cell) calculations of the $CaSnO_3$ *Pbnm* structure.

To calculate the formation energies of the defects, we also simulate bulk CuO and SnO_2 and the O_2 molecule using the same computational conditions as the ones adopted for the $CaSnO_3$ structure. Charge density integration for Bader analysis was performed adopting the most dense integration grid and including 10 shells of neighbors as possible attractors[58] whereas the default parameters were used in the Hirshfeld-I iterative procedure.[59] Further information on the structural models used is given in the subsection below.

Two different "removal" models are here adopted for oxygen vacancy formation: the first one is based on the complete removal of the atom and its basis set, hereafter called "atom removed" (AR), the second one involves the removal of the atom mass and charge but maintains its basis set, henceforth referred to as "ghost" (GH). We will discuss these two schemes when addressing the point of whether an oxygen vacancy in $CaSnO_3$ is neutral (*i.e.* possibly giving rise to an F-center) or not. To further check the correctness of our description, both models (AR and GH) are also used to describe an oxygen vacancy in the orthorhombic *Pbnm* $CaTiO_3$ perovskite with the same computational conditions. This is because this latter system is known to present an F-center, as other titanates and zirconates, and thus constitute an excellent benchmark to validate our approach.[60–64]

2.1 Structural models for oxygen vacancy and Cu doping in $CaSnO_3$

The primitive cell of the orthorhombic $CaSnO_3$ perovskite contains 4 formula units (20 atoms per cell). The cell contains two symmetry-independent oxygen atoms: one apical O_{ap} and one equatorial O_{eq}, that represent the two possible independent sites for the formation of an oxygen vacancy V_O. Both oxygen atoms bridge two tin atoms (Sn–O–Sn). At variance with cubic perovskites, the centro-symmetric orthorhombic structure is characterized by only 8 symmetry operators, out of which 6 are lost when the supercell is built so that the supercell only exhibits the inversion symmetry. This symmetry loss obviously increases the computational time of the corresponding calculations, and represents one of the reasons why perovskite-type materials have often been studied computationally employing cubic or pseudo-cubic structures.[60,63] When modeling the defects (oxygen vacancies or Cu doping) also the inversion symmetry is lost. A sketch of the structure of the $CaSnO_3$ perovskite and of the various defect configurations is given in Fig. 1.

The copper doping calculations require some special care: a reliable description of spin localization of the strongly-correlated unpaired d electrons of Cu centers can not be obtained with plain DFT formulations. Instead, self-interaction corrected formulations of DFT have to be used. In this respect, the most popular approaches to deal with strongly-correlated systems are the DFT+*U* or hybrid functionals.[66–68] The corresponding calculations are here performed with the hybrid PBE0 functional. We have considered two models for Cu doping: (i) the first one is simple substitution of tin by copper atoms, without further electronic compensation; and (ii) the second one is tin–copper substitution in the presence and vicinity of an oxygen vacancy. In the latter case, different structural models are considered with different relative positions of the Cu atom and the oxygen vacancy: (i) Cu as a first neighbor to the vacancy; (ii) Cu as a second neighbor to the vacancy with a connecting path of the type $Cu–O_{eq}–Sn–V_O$; and (iii) Cu as a third neighbor to the vacancy with a longer connecting path of the type $Cu–O_{eq}–Sn–V_O$.

The balanced charge and mass reactions investigated in this study are summarized in eqn (1)–(3) according to Kröger–Vink's notation:

$$\text{null} \xrightarrow{CaSnO_3} Sn''_{Sn} + V_O^{\bullet\bullet} + \frac{1}{2}O_{2(g)} \tag{1}$$

$$CuO + \frac{1}{2}O_{2(g)} \xrightarrow{CaSnO_3} Cu''_{Sn} + 2h^{\bullet} + SnO_2 \tag{2}$$

$$CuO \xrightarrow{CaSnO_3} Cu''_{Sn} + V_O^{\bullet\bullet} + SnO_2 \tag{3}$$

Eqn (1) refers to oxygen vacancy formation in pristine $CaSnO_3$, which is accompanied by electronic compensation due to the reduction of a tin ion formally from Sn^{4+} to Sn^{2+}. Eqn (2) refers to the simple substitution of a Sn atom by a Cu atom, compensated by the formation of two electron holes. Finally, eqn (3) refers to Cu-doping in the presence of an oxygen vacancy. It is worth pointing out that these are merely charge and mass balanced equations, using classical charge concepts, here displayed to facilitate the discussion.

Let us now briefly discuss some aspects of the electronic state of the various model structures. Pristine $CaSnO_3$ is a closed-shell system. We have studied the oxygen vacancy in

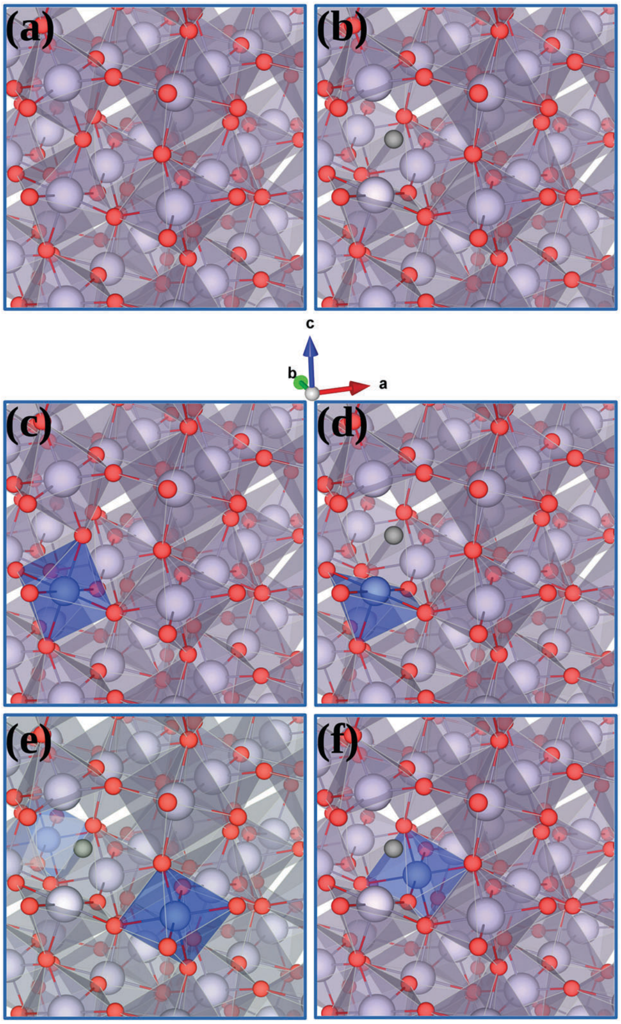

Fig. 1 Graphical representation of the structural models used for (a) the pristine $CaSnO_3$ perovskite, (b) the apical oxygen vacancy, (c) the Cu for Sn substitution, (d) Cu doping with the oxygen vacancy as a first neighbor, (e) Cu doping with the vacancy as a second neighbor, and (f) Cu doping with the vacancy as a third neighbor. Calcium atoms are not displayed for clarity. The oxygen vacancy is represented by a dark grey ball.[65]

three different ways: (i) as a closed-shell system with a spin-restricted formulation; (ii) as a singlet within a spin-unrestricted formulation; and (iii) as a triplet within a spin-unrestricted formulation. The most stable electronic configuration for an oxygen vacancy in $CaSnO_3$ is found to correspond to a closed-shell solution. We have studied all models for Cu-doping in terms of a spin-unrestricted formulation and found that the corresponding ground state is a spin-doublet. The spin-contamination of all explored electronic states has also been evaluated.

2.2 Electron charge analysis

As anticipated, the electron charge distribution of the system has been investigated according to four different partitioning schemes. Indeed, atomic charges do represent one of the most popular tools for the analysis of electron density. Obviously, the partitioning of the total electron density into atomic contributions is somewhat arbitrary and can be performed following different strategies that can be divided into two classes depending on whether they are based on the electron density itself or its molecular orbital representation. The simplest scheme belonging to the second class is the so-called Mulliken partition[69] in which atomic charges q depend on the periodic density P and overlap S matrix representations in the basis of atomic orbitals (AO) $\{\chi_\mu(\mathbf{r})\}$ as follows:

$$q_A = \sum_{\mu \in A} \sum_{\nu}^{M} \sum_{g}^{N} P^{g}_{\mu\nu} S^{g}_{\mu\nu} \tag{4}$$

where the second and third sums run over the M AOs of the reference cell and the N cells of the system, respectively. The first sum is restricted to the AOs centered on atom A.

The stockholder partition by Hirshfeld dissects the system into well-defined atomic fragments and the integration of $\rho(\mathbf{r})$ is weighted according to a general and natural choice, that is to share the charge density at each point among several atoms in proportion to their free-atom densities, at the corresponding distance from the nuclei.[74] The Hirshfeld-I method[73,75] has renewed the interest in the original scheme by eliminating the need for calculating the promolecular densities which are replaced with spherical symmetric weight functions, $w_A(\mathbf{r})$, optimized through an iterative procedure. The electronic population assigned to a center A is then obtained as

$$q_A = \int_{\Omega} w_A(\mathbf{r}) \rho(r) \mathrm{d}\mathbf{r} \tag{5}$$

Complementary to the analysis of atomic charges, two additional methods have been used to analyze the bonding pattern of the system: Bader's Quantum Theory of Atoms in Molecules (QTAIM),[70–72,92] and Wannier functions (*i.e.* localized crystalline orbitals).[76] From the QTAIM, critical points of the electron charge density are computed and characterized, according to which the occurrence and nature of chemical bonds can be discussed. Wannier functions provide information on where the localized crystalline orbitals are centered.

All these descriptors will be used to get an insight into the features of the electron charge distribution due to the formation of an oxygen vacancy in the $CaSnO_3$ lattice, with and without a Cu substitutional atom.

3 Results and discussion

Let us start by describing the density-of-states (DOS) of the orthorhombic $CaSnO_3$ perovskite, which will prove useful for the discussion to follow. The DOS of pristine $CaSnO_3$ is reported in Fig. 2. The contributions to the top of the valence band (VB) are mainly due to oxygen p states and the bottom of the conduction band (CB) to tin s and p states, in agreement with previous accounts.[77–80] The two oxygen types, O_{ap} and O_{eq}, contribute differently to the total DOS because of their different concentration (there are 4 O_{ap} and 8 O_{eq} in the unit cell). In their study of the $CH_3NH_3SnI_3$ orthorhombic perovskite, Bernal *et al.*[81]

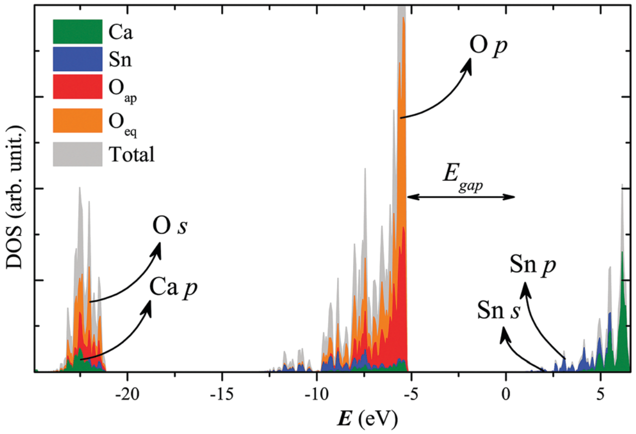

Fig. 2 Projected density-of-states of pristine CaSnO$_3$.

observed that relevant information on the oxidation state of Sn ions can be obtained from the analysis of the projected DOS. In particular, the presence of Sn s orbitals near the top of the VB suggests a formal Sn^{2+} reduced state while the presence of Sn s orbitals near the bottom of the CB suggests a formal Sn^{4+} full oxidation state. In our case, for the pristine CaSnO$_3$ perovskite, Sn s states are found at the bottom of the CB thus indicating a formal oxidation state of Sn^{4+}. A comprehensive orbital analysis of pristine CaSnO$_3$ has been performed by Mizogushi *et al.*[77] In the following, we will analyze how the presence of different kinds of defects affects the electronic DOS of the system. In particular, all of the investigated defects introduce new electronic energy levels (and thus some DOS) within the main band gap of the pristine system.

3.1 The oxygen vacancy

3.1.1 Structural aspects. The formation of an oxygen vacancy in the CaSnO$_3$ perovskite structure induces a series of structural and electronic modifications involving chemical bond breaking and rearrangement. Even though these effects propagate over a long range, they are clearly crucial for first and second neighbors. A detailed analysis of the structural changes induced by the formation of an oxygen vacancy, as obtained from full structural relaxations, is presented in Table S1 of the ESI.†

First of all, let us discuss the effect that the formation of an oxygen vacancy has on the cell volume. A low defect concentration has been investigated (1 oxygen atom out of 96 has been removed), which is consistent with experimental conditions,[82–85] so that the absolute volume change is small ($|\Delta V| = 0.1$–0.3%). However, the specific nature of the electronic state of the defect is found to have a significant impact on the kind of volumetric response: both a closed-shell singlet and a spin-unrestricted singlet state indeed produce a volume contraction ($\Delta V = -0.1\%$) while a spin-unrestricted triplet state, where the two unpaired electrons are forced to a spin-up configuration, results in a volume increase ($\Delta V = 0.3\%$). It is also seen that the formation of a vacancy in an O$_{eq}$ site results in a smaller structural deformation than in an O$_{ap}$ site. Indeed, the *c* crystallographic direction is known to be mechanically softer than the *a* and *b* ones, as recently investigated from anisotropic elastic calculations.[52,53] A recent experimental study also confirmed the importance of detailed directional analysis for CaSnO$_3$.[86] These structural effects turn out to be rather independent of the particular functional used (GGA or hybrid) as already suggested.[87–90]

3.1.2 Electron charge distribution. As recalled in the introduction, several ABO$_3$ perovskites exhibit F-centers upon oxygen vacancy formation (*i.e.* two electrons trapped in the vacancy). In order to check whether or not two electrons are hosted by the vacancy in CaSnO$_3$, we performed an analysis of the electron charge distribution with different approaches. Table S2 of the ESI† reports Mulliken and Hirshfeld-I atomic charges for the atoms surrounding the vacancy and the vacancy itself. Despite larger absolute values of the atomic charges obtained from the Hirshfeld-I scheme compared to the Mulliken one, both methods provide the same overall picture and trends. In particular, upon formation of the oxygen vacancy, the neighboring Sn atoms are found to be reduced by about 35% (*i.e.* their positive atomic charges decrease by about 35%). Furthermore, both approaches describe an "empty" vacancy with no electrons hosted. The electron density analysis performed on the closed-shell state and on the open-shell singlet state provides the same description, thus confirming that the ground state of this defect is indeed a closed-shell electronic configuration.

We also performed an analysis of the chemical bond pattern of the defective system based on Wannier functions (*i.e.* localized valence crystalline orbitals). From this analysis one gets information about where bond orbitals are centered, about what atoms are involved and about what charge they carry. The centroids of the bond Wannier functions around the vacancy are given in Fig. S1 of the ESI.† None of the obtained valence Wannier bond orbitals is found to involve the atomic functions centered in the middle of the vacancy but one corresponding to a covalent Sn–Sn bond with a tiny electron charge of 0.07 $|e|$ at the center, thus confirming the absence of an F-center. Let us stress that a similar type of bond has also been found for an oxygen vacancy in the inverse spinel Mg(Mg,Sn)O$_4$ structure.[91] The results of the Wannier analysis are found to be independent of the particular functional used and moreover show only little changes from the O$_{eq}$ to the O$_{ap}$ sites. In particular, when the vacancy is formed in an O$_{ap}$ site, the O$_{eq}$ sites become slightly more ionic while the other O$_{ap}$ site remains unchanged. The analysis of the degree of spatial localization of spin-up and spin-down electrons further confirms the higher stability of the singlet electronic state over the triplet one, which would be characterized by a very unbalanced electron distribution.

In order to further corroborate these findings and in particular the presence of a covalent Sn–Sn bond, we have performed a sophisticated topological analysis as proposed by Bader in the quantum theory of atoms in molecules (QTAIM). The analysis is performed with the PBE functional in the GH case. Bader's residual charge on the vacancy is found to be 0.098 $|e|$ and a bond critical point is found at the mid point between the two Sn atoms. According to all the usual descriptors of the QTAIM it is indeed a covalent bond: the Laplacian $\nabla^2\rho$ has a value of -0.008 a.u., the ratio of the potential energy over the positive definite kinetic energy $|V|/G$ of 3.04 and finally the ratio between the total electron energy and the density H/ρ of -0.166 a.u.[92]

The main purpose of the detailed analysis of the electron charge distribution in the defective system was that of checking whether or not an F-center would be formed in the $CaSnO_3$ perovskite upon removal of an oxygen atom. Clearly, the F-center does not arise in this system. Instead of being trapped at the center of the cavity, the two electrons reduce the neighboring Sn atoms (by about 35%), similar to eqn (1), and the vacancy is understood as a $V_O^{\bullet\bullet}$ type.[38–40]

3.1.3 Electronic structure. We now analyze the electronic structure of the defective system in terms of band structure and density-of-states. The band structure and the corresponding DOS of the defective system, with the oxygen vacancy in a singlet or triplet spin configuration, are reported in Fig. 3 along with those of the pristine system in order to highlight the electronic features introduced by the defect. The electronic states introduced by the defect are given in red. The pristine system is characterized by a wide band gap of about 5.6 eV at the PBE0 level of theory. The formation of an oxygen vacancy produces some electronic states with energy levels within the pristine energy band gap. In the singlet spin configuration (the most stable one; see discussion about the energetics in the section below), a doubly occupied energy level appears at about 2 eV above the top of the valence band of the pristine system, which reduces the band gap of the system to about 3.6 eV. The band structure of the triplet state is more complex with the formation of three states with energies within the pristine band gap, two occupied by unpaired spin-up electrons and one empty at just 0.5 eV above the highest occupied energy level. In all cases, the defect states are mainly due to s and p orbitals of the two Sn atoms that are first neighbors of the oxygen vacancy. This overall picture is almost independent of the particular site for oxygen substitution and of the way in which the vacancy is described (AR or GH). Furthermore, the same trends are obtained also with the PBE functional (obviously with different absolute values for the band gap).

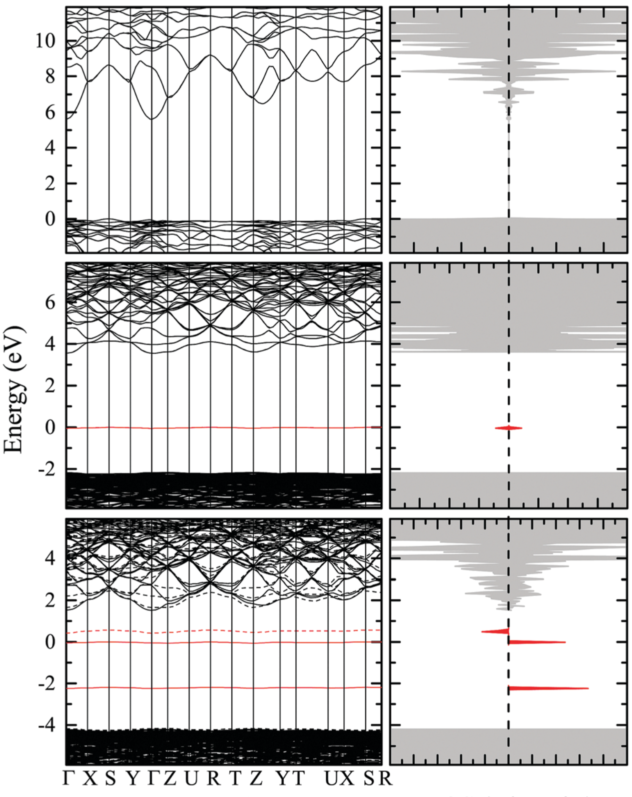

Fig. 3 Electronic band structure (left panels) and density-of-states (right panels) of pristine $CaSnO_3$ (top), and of the defective system with the oxygen vacancy in a singlet (middle) or triplet (bottom) spin configuration. In the DOS representation, spin up and spin down contributions are reported on the right and left of the vertical dashed line, respectively. The electronic states introduced by the defect are reported in red. For each system, the Fermi level is set to zero. Calculations were performed with the PBE0 functional.

3.1.4 Energetics. The energetics of the formation of an oxygen vacancy in the $CaSnO_3$ perovskite is illustrated in Table 1 as a function of the different electronic configurations of the defect. The last column of the table reports the electronic band gap E_g where it is seen that the formation of the oxygen vacancy results in a reduction of the pristine band gap by about 2 eV (from 5.6 to 3.6 eV). The triplet electronic state would imply a much lower value of just 0.5 eV as already discussed from the electronic band structures.

We have computed the formation energy E_f of the oxygen vacancy from the following reaction in our structural model that contains 160 atoms per cell in the pristine system:

$$Ca_{32}Sn_{32}O_{96} \rightarrow Ca_{32}Sn_{32}O_{95} + \frac{1}{2}O_{2(g)} \qquad (6)$$

Three calculations are needed: on the pristine system, on the defective perovskite and on the gas-phase oxygen molecule. From Table 1 we see that the closed-shell and singlet electronic configurations for the defect are almost energetically equivalent with formation energies of 5.23 and 5.22 eV, respectively. The triplet electronic state corresponds to a much higher formation energy of 7.02 eV, which implies a lower stability of the triplet configuration with respect to the singlet one by 1.8 eV. These values are consistent with those recently reported by Emery and Wolverton.[42] From our calculations, the formation of an oxygen vacancy in an equatorial site is found to be more energetically favored over that in an apical site by about 0.1 eV,

Table 1 Formation energy E_f, relaxation energy E_r and electronic energy band gap E_g (all in eV) of the oxygen vacancy in $CaSnO_3$ in different electronic spin configurations (closed-shell CS, singlet S and triplet T). Calculations were performed with the PBE0 hybrid functional

	E_r	E_f	E_g
Pristine	—	—	5.6
Exp.[77]	—	—	4.4
O vacancy (CS)	−0.33	5.23	3.6
O vacancy (S)	−0.33	5.22	3.6
O vacancy (T)	−0.23	7.02	0.5

which is in agreement with what is reported for the $CaZrO_3$ perovskite.[93] Let us stress that, from these static electronic calculations (*i.e.* performed at 0 K), the formation of the oxygen vacancy would be energetically not favored. We will discuss explicitly the effect of temperature on the formation energy of the defect below.

Table 1 also reports the relaxation energy E_r defined as the energy gain due to full structural relaxation upon vacancy creation. This quantity basically quantifies the amount of structural relaxation induced by the formation of the defect. We observe that the structural relaxation is more evident when the defect is in the singlet state; the higher electron–electron repulsion of the triplet configuration indeed does not allow for relaxation as large as for the singlet configuration. Furthermore, the triplet state is found to be more "spin contaminated" than the singlet one. Indeed, in principle, the electronic states obtained from unrestricted Kohn–Sham DFT calculations are not guaranteed to be eigenstates of the $\hat{S}^2$ operator. The spin contamination ΔS can be computed as the difference between the actual value of the expectation value of this operator and the ideal expectation value $\Delta S = \langle \hat{S}^2 \rangle - \langle \hat{S}^2 \rangle_{\text{ideal}}$. For singlet and triplet states, $\langle \hat{S}^2 \rangle_{\text{ideal}}$ would be 0 and 2, respectively. No spin contamination is found for the singlet state while a spin contamination of 0.005 is obtained for the triplet state.

3.1.5 Thermodynamics. In order to take into account thermal effects on the formation energy of an oxygen vacancy in the $CaSnO_3$ perovskite, and, at the same time, in order to check the effect of the vacancy on some thermodynamic properties of the system, we have computed harmonic vibration frequencies of the pristine and of the defective supercell (containing 160 and 159 atoms) systems. The size of the adopted supercell is such to ensure full convergence of the harmonic thermodynamic properties with respect to the sampling of the phonon dispersion. Given the high computational cost of these calculations, the PBE functional has been used in this case. Fig. 4 reports the constant-volume specific heat C_v (left panel) and the vibrational entropy (right panel) as a function of temperature as obtained for the pristine system (dashed lines) and for the defective system (continuous lines). It is seen that the formation of an oxygen vacancy in the $CaSnO_3$ perovskite structure increases its specific heat by about $\Delta C_v = 21$ J (mol K)$^{-1}$ in a wide temperature range (from room temperature up to its melting temperature) and increases its vibrational entropy, ΔS, by an amount that increases with temperature. These values are reported in Table 2 for selected temperatures. In the same table, we also report the computed Gibbs formation free energy of the oxygen vacancy that we have obtained by considering the formation reaction (7) and by working in terms of the Gibbs free energy and no longer in terms of the static purely electronic energy. From the table, it is seen that, as temperature increases, the formation of the oxygen vacancy becomes more energetically favorable. Above about 800 K the formation of the defect becomes spontaneous. For a detailed account of the calculation of defect formation free energies the reader is addressed to ref. 94 and 95.

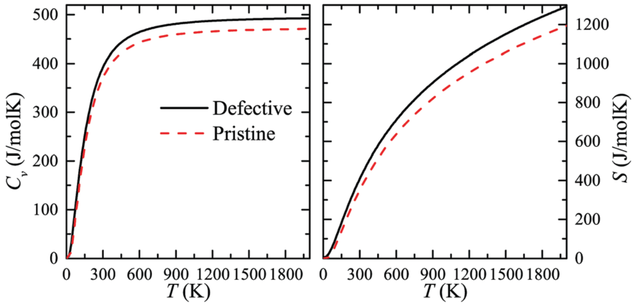

Fig. 4 Constant-volume specific heat (left panel) and entropy (right panel) of the $CaSnO_3$ perovskite without (dashed line) and with the oxygen vacancy (continuous line). The calculation is performed with the PBE functional.

Table 2 Gibbs free energy of formation ΔG_f of the oxygen vacancy in $CaSnO_3$ as a function of temperature. The variations of the constant-volume specific heat ΔC_v and vibrational entropy ΔS of the system due to the vacancy formation are also reported. Thermodynamic properties are obtained from PBE harmonic frequencies

T (K)	ΔG_f (eV)	ΔC_v [J (mol K)$^{-1}$]	ΔS [J (mol K)$^{-1}$]
0	4.78	—	—
300	3.57	21.38	57.93
600	1.60	21.58	72.80
900	−0.68	21.70	81.58
1200	−3.16	21.75	87.83
1800	−8.53	21.79	96.65

3.1.6 $CaTiO_3$. As illustrated before, all indicators suggest that no F-center is created in the $CaSnO_3$ perovskite upon formation of an oxygen vacancy: electrons are not trapped in the vacancy but rather reduce the neighboring Sn atoms. On the contrary, an F-center is known to occur in the isostructural orthorhombic $CaTiO_3$ perovskite. In order to check the reliability of our quantum-mechanical calculations, we have also investigated the oxygen vacancy in $CaTiO_3$. In this case, a significant electron density is localized in the vacancy (F-center) and the most stable electronic configuration is the triplet state and no longer the singlet state as in $CaSnO_3$. The energy difference between the AR and the GH description of the vacancy (without and with basis functions centered on the vacancy, respectively) was just 0.2 eV for $CaSnO_3$ while it is 1.11 eV for $CaTiO_3$, which further confirms the need of those functions on the vacancy because of the residual electron density on that site. The electronic band structures of the different spin configurations of the oxygen vacancy in $CaTiO_3$ are reported in the ESI.† Moreover, the 3D representation of the spin density of the most stable triplet case is also given in the ESI.†

3.2 Cu doping

We have already described the structural models that we have used to investigate the effect of Cu doping in $CaSnO_3$. In particular, we have studied the substitution of a single Sn atom by a Cu atom (*i.e.* from SnO_6 to CuO_6) without or with an oxygen vacancy in its spatial vicinity. When the oxygen vacancy and the Cu substitution are both present, different relative distances are considered: the Cu atom can be a first, second or third neighbor to the vacancy.

Table S3 of the ESI† illustrates the structural changes induced by Cu doping in the $CaSnO_3$ perovskite with and without an oxygen vacancy. The most evident structural change occurring upon substitution is the elongation of the two Cu–O apical bonds in the CuO_6 octahedron, which produces a local distortion towards a planar CuO_4 configuration. The Sn to Cu substitution alone (without an oxygen vacancy) results in a decrease of the cell volume ($\Delta V = -0.4\%$). Also the case in which a Cu atom is inserted as a first neighbor to the oxygen vacancy results in an overall decrease of the cell volume ($\Delta V = -0.15\%$) with respect to the pristine system. However, we observe that, when the Cu atom is a second or third neighbor to the vacancy, the cell volume slightly increases ($\Delta V = 0.04$–0.09%) with respect to the pristine system.

The Cu atom is in a d^9 electronic configuration so that it hosts one unpaired electron. Fig. 5 reports the spin density of the different models considered for Cu doping and clearly shows that the unpaired electron is always very localized on the Cu and on some of its first neighbors. In particular, the (a) panel corresponds to the case where there is no oxygen vacancy: the unpaired electron is mainly hosted in the CuO_4 plane with some spin density also on the two apical oxygen atoms corresponding to more elongated bonds. Panel (b) shows how higher spin localization in the CuO_4 plane is achieved when one of the two apical oxygen atoms is removed to form a vacancy (the site of the vacancy is represented as a small dark grey ball). Panels (c) and (d) show the spin localization when the Cu atom is a second and third neighbor of the vacancy, respectively. Because of the unpaired electron on the Cu center, all investigated configurations are treated as spin doublets with ideal values of $\langle \hat{S}^2 \rangle_{\text{ideal}} = 0.75$. The highest spin contamination (0.039) is found for the Cu doping case without any oxygen vacancy while the other cases are characterized by a much lower contamination of 0.003, 0.003 and 0.002, respectively.

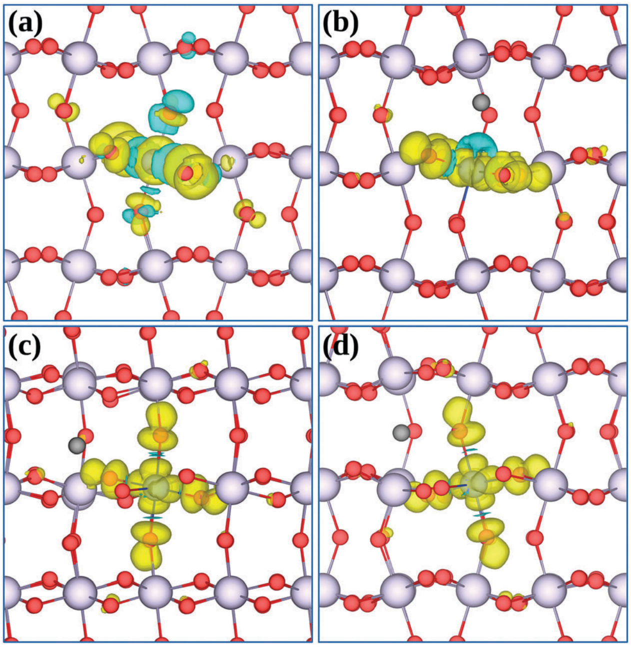

Fig. 5 Spin density 3D maps (cutoff 0.001 e $bohr^{-3}$) for (a) Cu substitution without an oxygen vacancy (b) the Cu atom as a first neighbor to the vacancy (c) the Cu atom as a second neighbor to the vacancy, and (d) the Cu atom as a third neighbor to the vacancy. The site of the vacancy is represented as a small dark grey ball. Calculations were performed with the PBE0 hybrid functional.

As observed in the case of the oxygen vacancy alone, also in the presence of Cu doping, the vacancy is found not to host electrons. The Mulliken and Hirshfeld-I analysis of the electron charge distribution for Cu doping is given in Table S4 of the ESI.† The effect on the atomic charges of oxygen vacancy formation in the presence of a Cu substitutional atom is as follows: while in the non-doped system, the vacancy produces a reduction of the Sn atomic charge by about 35% (see above), now the Sn charge is reduced only by about 7%. This is due to the fact that the Cu atom and its neighboring oxygen atoms are hosting a large fraction of the extra electrons. Indeed, the atomic charge of Cu reduces by about 25% while those of its neighboring oxygen atoms increase by about 10% in absolute value (with a larger change by about 18% for the apical oxygen atom). We have analyzed the chemical bonding in Cu-substituted $CaSnO_3$ by means of localized Wannier functions and of Bader's QTAIM. Both approaches reveal that, in variance with the case of the oxygen vacancy alone, no metal–metal bond is formed in the presence of Cu substitution. Not only no Cu–Sn bond is observed when the Cu atom is a first neighbor of the vacancy, but no Sn–Sn bond is observed when the Cu is a second or third neighbor of the vacancy. This confirms that the origin of the covalent Sn–Sn bond when there is the oxygen vacancy alone is due to the induced reduction of the Sn sites close to the vacancy. In the absence of a vacancy, the six Cu–O bonds are found to be more covalent than in the presence of the vacancy. In particular, when the vacancy is a first neighbor to the Cu atom, the four equatorial Cu–O bonds are characterized by a much higher ionicity.

The electronic band structure and corresponding density-of-states of the various configurations of Cu doping here considered are given in Fig. 6: the Cu doped $CaSnO_3$ perovskite without an oxygen vacancy (top), with the oxygen vacancy as a first neighbor of the Cu atom (middle) and as a second neighbor (bottom). It is seen that, in all cases, the Sn substitution for Cu creates some electronic states whose energy falls within the pristine gap. This is particularly so when no oxygen vacancy is present. Copper states at the top of the valence band are formed as well as states within the pristine gap, which overall result in a small electronic energy gap of just 1.8 eV (compared to the gap of 5.6 eV of the pristine system). When the Cu atom is a first or second neighbor to the oxygen vacancy, the electronic structure is affected differently: some extra density-of-states builds up near the top of the valence band (mainly arising from p oxygen orbitals and d_{z^2} and d_{xy} copper orbitals) and near the bottom of the conduction band (mainly arising from d_{xy} copper orbitals and s and p tin orbitals), resulting in a smaller reduction of the band gap to 4.2 and 3.6 eV, respectively. The presence of copper d states within the pristine gap is relevant to potential catalytic applications.[96–99] The values of the electronic energy band gap E_g of the different configurations of Cu doping are given in Table 3.

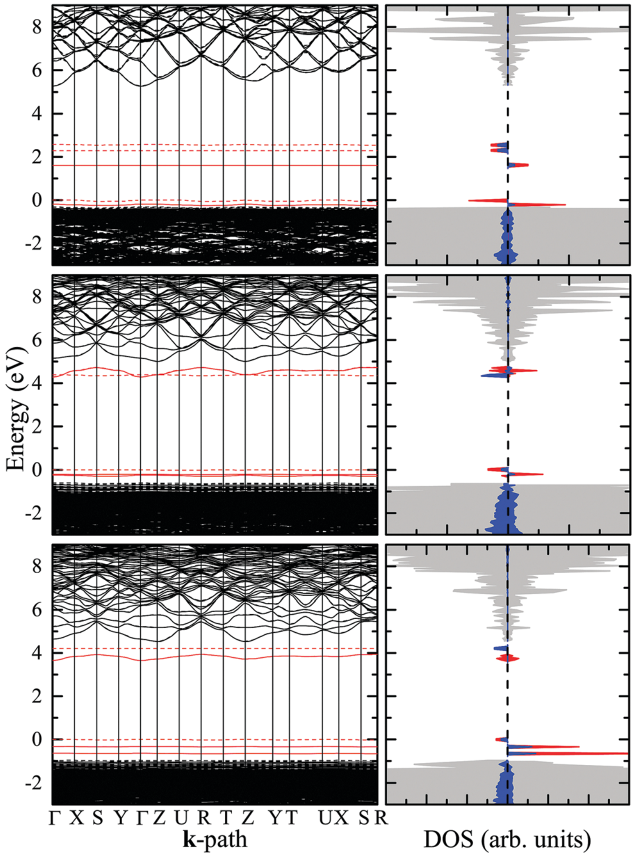

Fig. 6 Electronic band structure (left panels) and density-of-states (right panels) of the Cu doped $CaSnO_3$ perovskite without an oxygen vacancy (top), with the oxygen vacancy as a first neighbor of the Cu atom (middle) and as a second neighbor (bottom). In the DOS representation, spin up and spin down contributions are reported on the right and left of the vertical dashed line, respectively. The electronic states introduced by the defect are reported in red (the contribution of Cu is represented in blue). For each system, the Fermi level is set to zero. Calculations were performed with the PBE0 functional.

The energetics of the different doping configurations is given in Table 3. The relaxation energy E_r tells us that the smallest structural relaxation occurs when the Cu substitution is done without any oxygen vacancy. When a neighboring oxygen vacancy is present, the structure undergoes a larger structural relaxation as the relative distance of the Cu center and the vacancy increases. This is due to the fact that when the Cu atom is a first neighbor to the vacancy, the metal–metal covalent bond is not formed. We have also evaluated the formation energy E_f of the different defects. The reaction used to compute the formation energy of the simple Sn for Cu substitution is:

$$Ca_{32}Sn_{32}O_{96} + CuO + \frac{1}{2}O_{2(g)} \rightarrow Ca_{32}Sn_{31}Cu_1O_{96} + SnO_2$$

while the reaction considered for the simultaneous Cu substitution and oxygen vacancy creation is:

$$Ca_{32}Sn_{32}O_{96} + CuO \rightarrow Ca_{32}Sn_{31}CuO_{95} + SnO_2$$

It proves convenient to evaluate the formation energy of the oxygen vacancy where the reference system is the Cu-doped $CaSnO_3$ perovskite. We compute the formation energy E_f^{Cu} of the oxygen vacancy in the Cu-doped system from the following reaction in our structural model that contains 160 atoms per cell in the pristine system:

$$Ca_{32}Sn_{31}Cu_1O_{96} \rightarrow Ca_{32}Sn_{31}Cu_1O_{95} + \frac{1}{2}O_{2(g)} \qquad (7)$$

Values for E_f^{Cu} are given in Table 3. Comparison with Table 1 clearly shows that the formation of an oxygen vacancy in the Cu-doped system is much more energetically favorable than in the pristine $CaSnO_3$ system, particularly so when the vacancy is a first neighbor of the Cu substitutional atom (in this case, the formation of an oxygen vacancy is found to be spontaneous also without thermal effects).

Table 3 Formation energy E_f, relaxation energy E_r and electronic energy band gap E_g (all in eV) of Sn for Cu substitution in $CaSnO_3$ without and with a neighboring oxygen vacancy. The formation energy E_f^{Cu} of the oxygen vacancy in the Cu-doped system is also reported. Calculations were performed with the PBE0 hybrid functional

	E_r	E_f	E_f^{Cu}	E_g
Pristine	—	—	—	5.6
Exp.[77]	—	—	—	4.4
Cu (no vacancy)	−0.47	3.33	—	1.8
Cu (first neighbor)	−2.17	3.01	−0.33	4.2
Cu (second neighbor)	−2.31	4.46	1.13	3.6
Cu (third neighbor)	−2.42	4.44	1.10	3.7

Energetically, the most stable defect configuration is represented by an oxygen vacancy a first neighbor of the Cu atom, which confirms the tendency of defects with opposite local charges to associate.[100–102]

4 Conclusions

We have performed density functional theory (DFT) calculations on large structural models to investigate the structural, electronic, energetic, and thermodynamic properties of two point-defects in the $CaSnO_3$ perovskite. Hybrid functionals of DFT have been used, which by including a fraction of exact non-local Fock exchange allow for a reliable description of spin polarized systems.

At variance with what is observed in other ABO_3 perovskites (and notably in $CaTiO_3$), no F-center is created upon formation of an oxygen vacancy in $CaSnO_3$. The two electrons are not "trapped" into the vacancy but rather reduce the neighboring Sn atoms. A Sn–Sn covalent bond is formed bridging the oxygen vacancy. The most stable electronic configuration of the oxygen vacancy defect in $CaSnO_3$ is a singlet, while the triplet polarized state is higher in energy by about 1.8 eV. The formation of the oxygen defect is predicted to significantly affect (increase) the specific heat of the system and to become energetically spontaneous above about 800 K.

Upon substitution of an Sn atom by a Cu one in the octahedral site, the local octahedral site symmetry is distorted to induce a planar CuO_4 configuration with two apical elongated Cu–O bonds. The copper substitution is found to largely reduce the electronic band gap of the system (by about 3.8 eV). The combination of the two defects has also been investigated, according to which the configuration in which the oxygen vacancy is a first neighbor of the Cu atom is found to be the most stable one.

Conflicts of interest

There are no conflicts to declare.

Acknowledgements

J. M. acknowledges the Brazilian scholarship program "Ciência sem Fronteiras" (Process Number 248425/2013-7/SWE), the Center for Scientific Computing of the São Paulo State University (GridUNESP) and the support of the Modeling and Molecular Simulations Group UNESP-Bauru. Furthermore, we are grateful for the programs PROCAD 2013/Proc. 88881.068492/2014-01, FAPESP 07476-9 and CNPq 46126-4. We also would like to thank Prof. R. Orlando and Prof. R. Dovesi for their contributions on the early stages of this study and Prof. C. M. Zicovich-Wilson with whom J. M. developed much of this study in 2016 at the Centro de Investigación en Ciencias, Universidad Autónoma del Estado de Morelos – Mexico.

References

1 M. A. Peña and J. L. G. Fierro, *Chem. Rev.*, 2001, **101**, 1981–2018.

2 A. Kubacka, M. Fernández-García and G. Colón, *Chem. Rev.*, 2012, **112**, 1555–1614.

3 R. Thalinger, A. K. Opitz, S. Kogler, M. Heggen, D. Stroppa, D. Schmidmair, R. Tappert, J. Fleig, B. Klötzer and S. Penner, *J. Phys. Chem. C*, 2015, **119**, 11739–11753.

4 L. An and H. Onishi, *ACS Catal.*, 2015, **5**, 3196–3206.

5 E. N. Armstrong, K. L. Duncan and E. D. Wachsman, *Phys. Chem. Chem. Phys.*, 2013, **15**, 2298–2308.

6 M. Misono, *Heterogeneous Catalysis of Mixed Oxides Perovskite and Heteropoly Catalysts*, 2013, vol. 176, pp. 67–95.

7 X. Y. Meng, D. Y. Liu and G. W. Qin, *Energy Environ. Sci.*, 2018, **11**, 692–701.

8 J. K. Stolarczyk, S. Bhattacharyya, L. Polavarapu and J. Feldmann, *ACS Catal.*, 2018, **8**, 3602–3635.

9 K. Ueda and Y. Shimizu, *Thin Solid Films*, 2010, **518**, 3063–3066.

10 T. Nakamura, M. Shima, M. Yasukawa and K. Ueda, *J. Sol-Gel Sci. Technol.*, 2012, **61**, 362–366.

11 J. Zhang, B. Chen, Z. Liang, X. Li, J. Sun, L. Cheng and H. Zhong, *J. Alloys Compd.*, 2014, **612**, 204–209.

12 S.-D. Kim, K.-S. Hwang and S. Hwangbo, *Electron. Mater. Lett.*, 2013, **9**, 405–407.

13 K. S. Hwang, Y. S. Jeoni, S. Hwangbo and J. T. Kim, *Ceram. Int.*, 2013, **39**, 8555–8558.

14 K. Ueda, T. Maeda, K. Nakayashiki, K. Goto, Y. Nakachi, H. Takashima, K. Nomura, K. Kajihara and H. Hosono, *Appl. Phys. Express*, 2008, **1**, 015003.

15 F. Zhong, H. Zhuang, Q. Gu and J. Long, *RSC Adv.*, 2016, **6**, 42474–42481.

16 Y. Karabulut, M. Ayvackl, A. Canimoglu, J. Garcia Guinea, Z. Kotan, E. Ekdal, O. Akyuz and N. Can, *Spectrosc. Lett.*, 2014, **47**, 630–641.

17 V. Orsi Gordo, Y. Tuncer Arslanli, A. Canimoglu, M. Ayvacikli, Y. Galvão Gobato, M. Henini and N. Can, *Appl. Radiat. Isot.*, 2015, **99**, 69–76.

18 A. Canimoglu, J. Garcia-Guinea, Y. Karabulut, M. Ayvacikli, A. Jorge and N. Can, *Appl. Radiat. Isot.*, 2015, **99**, 138–145.

19 M. Suzuki and T. Murakami, *Solid State Commun.*, 1985, **53**, 691–694.

20 L. Buannic, F. Blanc, D. S. Middlemiss and C. P. Grey, *J. Am. Chem. Soc.*, 2012, **134**, 14483–14498.

21 A. M. Ritzmann, A. B. Muñoz-García, M. Pavone, J. A. Keith and E. A. Carter, *Chem. Mater.*, 2013, **25**, 3011–3019.

22 A. M. Deml, V. Stevanoviić, A. M. Holder, M. Sanders, R. O'Hayre and C. B. Musgrave, *Chem. Mater.*, 2014, **26**, 6595–6602.

23 I. Kagomiya, K. Jimbo, K.-I. Kakimoto, M. Nakayama and O. Masson, *Phys. Chem. Chem. Phys.*, 2014, **16**, 10875–10882.

24 K. Eom, E. Choi, M. Choi, S. Han, H. Zhou and J. Lee, *J. Phys. Chem. Lett.*, 2017, **8**, 3500–3505.

25 A. L. Gavin and G. W. Watson, *Phys. Chem. Chem. Phys.*, 2017, **19**, 24636–24646.

26 I. Bredeson, L. Zhang, P. R. C. Kent, V. R. Cooper and H. Xu, *Phys. Rev. Mater.*, 2018, **2**, 035401.

27 M. Asa, G. Vinai, J. L. Hart, C. Autieri, C. Rinaldi, P. Torelli, G. Panaccione, M. L. Taheri, S. Picozzi and M. Cantoni, *Phys. Rev. Mater.*, 2018, **2**, 033401.

28 H. Takahashi, I. Oikawa and H. Takamura, *J. Phys. Chem. C*, 2018, **122**, 6501–6507.

29 L. Zhang, S. Wang and C. Lu, *Anal. Chem.*, 2015, **87**, 7313–7320.

30 K. Tang, A. C. Meng, F. Hui, Y. Shi, T. Petach, C. Hitzman, A. L. Koh, D. Goldhaber-Gordon, M. Lanza and P. C. McIntyre, *Nano Lett.*, 2017, **17**, 4390–4399.

31 S. Huygh, A. Bogaerts and E. C. Neyts, *J. Phys. Chem. C*, 2016, **120**, 21659–21669.

32 J. A. Dawson, H. Chen and I. Tanaka, *J. Phys. Chem. C*, 2014, **118**, 14485–14494.

33 A. Zorko, M. Pregelj, H. Luetkens, A.-K. Axelsson and M. Valant, *Phys. Rev. B: Condens. Matter Mater. Phys.*, 2014, **89**, 094418.

34 N. Kitamura, J. Akola, S. Kohara, K. Fujimoto and Y. Idemoto, *J. Phys. Chem. C*, 2014, **118**, 18846–18852.

35 M. Ito, M. Uchida, Y. Kozuka, K. S. Takahashi and M. Kawasaki, *Phys. Rev. B*, 2016, **93**, 045139.

36 S. Lee, H. Wang, P. Gopal, J. Shin, H. M. I. Jaim, X. Zhang, S.-Y. Jeong, D. Usanmaz, S. Curtarolo, M. Fornari, M. B. Nardelli and I. Takeuchi, *Chem. Mater.*, 2017, **29**, 9378–9385.

37 S. Sumithra and N. V. Jaya, *J. Mater. Sci.: Mater. Electron.*, 2018, **29**, 4048–4057.

38 D. Gryaznov, S. Baumann, E. A. Kotomin and R. Merkle, *J. Phys. Chem. C*, 2014, **118**, 29542–29553.

39 M. M. Kuklja, Y. A. Mastrikov, B. Jansang and E. A. Kotomin, *J. Phys. Chem. C*, 2012, **116**, 18605–18611.

40 D. Gryaznov, E. Blokhin, A. Sorokine, E. A. Kotomin, R. A. Evarestov, A. Bussmann-Holder and J. Maier, *J. Phys. Chem. C*, 2013, **117**, 13776–13784.

41 V. S. Urusov and E. V. Leonenko, *Mineral. J.*, 2012, 3–11.

42 A. A. Emery and C. Wolverton, *Sci. Data*, 2017, **4**, 170153.

43 L. Weston, L. Bjaalie, K. Krishnaswamy and C. G. Van de Walle, *Phys. Rev. B*, 2018, **97**, 054112.

44 S. Zhang, P. Zhang, Y. Wang, Y. Ma, J. Zhong and X. Sun, *ACS Appl. Mater. Interfaces*, 2014, **6**, 14975–14980.

45 A. Johari, A. Johari, M. C. Bhatnagar and M. Sharma, *J. Nanosci. Nanotechnol.*, 2014, **14**, 5288–5292.

46 C. M. Ghimbeu, M. Lumbreras, M. Siadat, R. C. van Landschoot and J. Schoonman, *Sens. Actuators, B*, 2008, **133**, 694–698.

47 A. D. Garje, A. Inamdar and R. C. Aiyer, *Int. J. Appl. Ceram. Technol.*, 2011, **8**, 691–699.

48 M. J. Fuller and M. E. Warwick, *J. Catal.*, 1974, **34**, 445–453.

49 R. Dovesi, R. Orlando, A. Erba, C. M. Zicovich-Wilson, B. Civalleri, S. Casassa, L. Maschio, M. Ferrabone, M. De La Pierre, P. D'Arco, Y. Noël, M. Causá, M. Rérat and B. Kirtman, *Int. J. Quantum Chem.*, 2014, **114**, 1287–1317.

50 R. Dovesi, A. Erba, R. Orlando, C. M. Zicovich-Wilson, B. Civalleri, L. Maschio, M. Rérat, S. Casassa, J. Baima, S. Salustro and B. Kirtman, *Wiley Interdiscip. Rev.: Comput. Mol. Sci.*, 2018, e1360.

51 A. Erba, J. Baima, I. Bush, R. Orlando and R. Dovesi, *J. Chem. Theory Comput.*, 2017, **13**, 5019–5027.

52 J. Maul, A. Erba, I. M. G. Santos, J. R. Sambrano and R. Dovesi, *J. Chem. Phys.*, 2015, **142**, 014505.

53 J. Maul, I. M. G. Santos, J. R. Sambrano and A. Erba, *Theor. Chem. Acc.*, 2016, **135**, 1–9.

54 K. Doll and N. Harrison, *Chem. Phys. Lett.*, 2000, **317**, 282–289.

55 J. P. Perdew, K. Burke and M. Ernzerhof, *Phys. Rev. Lett.*, 1996, **77**, 3865–3868.

56 C. Adamo and V. Barone, *J. Chem. Phys.*, 1999, **110**, 6158–6170.

57 R. Dovesi, V. R. Saunders, C. Roetti, R. Orlando, C. M. Zicovich-Wilson, F. Pascale, B. Civalleri, K. Doll, N. M. Harrison, I. J. Bush, P. D'Arco, M. Llunell, M. Causà and Y. Noël, *CRYSTAL14 User's Manual*, 2014.

58 C. Gatti and S. Casassa, *TOPOND-2013: An Electron Density Topological Program For Systems Periodic In N (N = 0-3) Dimensions, User's Manual*, CNR-CSRSRC, Milano, 2013.

59 R. Dovesi, V. R. Saunders, C. Roetti, R. Orlando, C. M. Zicovich-Wilson, F. Pascale, B. Civalleri, K. Doll, N. M. Harrison, I. J. Bush, P. D'Arco, M. Llunell, M. Causà, Y. Noel, L. Maschio, A. Erba, M. Rerat and S. Casassa, *CRYSTAL 2017 User's Manual*, 2017.

60 R. I. Eglitis, E. A. Kotomin and G. Borstel, *Comput. Mater. Sci.*, 2004, **30**, 376–382.

61 P. G. Sundell, M. E. Björketun and G. Wahnström, *Phys. Rev. B: Condens. Matter Mater. Phys.*, 2006, **73**, 104112.

62 W.-J. Yin, S.-H. Wei, M. M. Al-Jassim and Y. Yan, *Phys. Rev. B: Condens. Matter Mater. Phys.*, 2012, **85**, 201201.

63 R. I. Eglitis, *Int. J. Mod. Phys. B*, 2014, **28**, 1430009.

64 T. S. Bjørheim, M. Arrigoni, D. Gryaznov, E. Kotomin and J. Maier, *Phys. Chem. Chem. Phys.*, 2015, **17**, 20765–20774.

65 K. Momma and F. Izumi, *J. Appl. Crystallogr.*, 2011, **44**, 1272–1276.

66 Y. Maimaiti, M. Nolan and S. D. Elliott, *Phys. Chem. Chem. Phys.*, 2014, **16**, 3036–3046.

67 A. K. Mishra, A. Roldan and N. H. de Leeuw, *J. Phys. Chem. C*, 2016, **120**, 2198–2214.

68 K. E. El-Kelany, C. Ravoux, J. K. Desmarais, P. Cortona, Y. Pan, J. S. Tse and A. Erba, *Phys. Rev. B*, 2018, **97**, 245118.

69 R. S. Mulliken, *J. Chem. Phys.*, 1955, **23**, 1841.

70 R. F. W. Bader, *Atoms in Molecules – A Quantum Theory*, Oxford University Press, Oxford, UK, 1990.

71 C. Gatti, V. R. Saunders and C. Roetti, *J. Chem. Phys.*, 1994, **101**, 10686.

72 S. Casassa, A. Erba, J. Baima and R. Orlando, *J. Comput. Chem.*, 2015, **36**, 1940–1946.

73 C. M. Zicovich-Wilson, M. Hô, A. M. Navarrete-López and S. Casassa, *Theor. Chem. Acc.*, 2016, **135**, 188.

74 F. L. Hirshfeld, *Theor. Chim. Acta*, 1977, **44**, 129.

75 P. Bultinck, C. V. Alsenoy, P. W. Ayers and R. Carbó-Dorca, *J. Chem. Phys.*, 2007, **126**, 144111.

76 C. M. Zicovich-Wilson, R. Dovesi and V. R. Saunders, *J. Chem. Phys.*, 2001, **115**, 9708–9719.

77 H. Mizoguchi, H. W. Eng and P. M. Woodward, *Inorg. Chem.*, 2004, **43**, 1667–1680.

78 J. M. Henriques, E. W. S. Caetano, V. N. Freire, J. A. P. da Costa and E. L. Albuquerque, *J. Phys.: Condens. Matter*, 2007, **19**, 106214.

79 W. Zhang, J. Tang and J. Ye, *J. Mater. Res.*, 2007, **22**, 1859–1871.

80 D. Cherrad, M. Maouche, M. Maamache and L. Krache, *Physica B*, 2011, **406**, 2714–2722.

81 C. Bernal and K. Yang, *J. Phys. Chem. C*, 2014, **118**, 24383–24388.

82 J. A. M. Van Roosmalen and E. H. P. Cordfunke, *J. Solid State Chem.*, 1991, **93**, 212–219.

83 Z. Q. Liu, D. P. Leusink, X. Wang, W. M. Lü, K. Gopinadhan, A. Annadi, Y. L. Zhao, X. H. Huang, S. W. Zeng, Z. Huang, A. Srivastava, S. Dhar, T. Venkatesan and Ariando, *Phys. Rev. Lett.*, 2011, **107**, 146802.

84 R.-A. Eichel, *Phys. Chem. Chem. Phys.*, 2011, **13**, 368–384.

85 H. Tan, Z. Zhao, W.-B. Zhu, E. N. Coker, B. Li, M. Zheng, W. Yu, H. Fan and Z. Sun, *ACS Appl. Mater. Interfaces*, 2014, **6**, 19184–19190.

86 J. D. Baniecki, T. Yamazaki, D. Ricinschi, Q. Van Overmeere, H. Aso, Y. Miyata, H. Yamada, N. Fujimura, R. Maran, T. Anazawa, N. Valanoor and Y. Imanaka, *Sci. Rep.*, 2017, **7**, 41725.

87 A. Erba, J. Maul, R. Demichelis and R. Dovesi, *Phys. Chem. Chem. Phys.*, 2015, **17**, 11670–11677.

88 A. Erba, J. Maul, M. De La Pierre and R. Dovesi, *J. Chem. Phys.*, 2015, **142**, 204502.

89 A. Erba, J. Maul, M. Itou, R. Dovesi and Y. Sakurai, *Phys. Rev. Lett.*, 2015, **115**, 117402.

90 A. Erba, J. Maul and B. Civalleri, *Chem. Commun.*, 2016, **52**, 1820–1823.

91 G. K. Behrh, M. Isobe, F. Massuyeau, H. Serier-Brault, E. E. Gordon, H.-J. Koo, M.-H. Whangbo, R. Gautier and S. Jobic, *Chem. Mater.*, 2017, **29**, 1069–1075.

92 S. Casassa, A. Erba, J. Baima and R. Orlando, *J. Comput. Chem.*, 2015, **36**, 1940–1946.

93 S. M. Alay-e Abbas, S. Nazir, S. Cottenier and A. Shaukat, *Sci. Rep.*, 2017, **7**, 8439.

94 K. Reuter and M. Scheffler, *Phys. Rev. B: Condens. Matter Mater. Phys.*, 2001, **65**, 035406.

95 U. Aschauer, R. Pfenninger, S. M. Selbach, T. Grande and N. A. Spaldin, *Phys. Rev. B: Condens. Matter Mater. Phys.*, 2013, **88**, 054111.

96 N. Kumagai, L. Ni and H. Irie, *Chem. Commun.*, 2011, **47**, 1884–1886.

97 K. J. Pyper, J. E. Yourey and B. M. Bartlett, *J. Phys. Chem. C*, 2013, **117**, 24726–24732.

98 T. Wang, X. Yan, S. Zhao, B. Lin, C. Xue, G. Yang, S. Ding, B. Yang, C. Ma, G. Yang and G. Yang, *J. Mater. Chem. A*, 2014, **2**, 15611–15619.

99 H. Yaghoubi, Z. Li, Y. Chen, H. T. Ngo, V. R. Bhethanabotla, B. Joseph, S. Ma, R. Schlaf and A. Takshi, *ACS Catal.*, 2015, **5**, 327–335.

100 Y.-M. Chiang, W. D. Kingery and D. P. Birnie, *Physical Ceramics: Principles for Ceramic Science and Engineering*, John Wiley& Sons Inc., 1996.

101 E. Ebsworth, A. Maddock and A. Sharpe, *New Pathways in Inorganic Chemistry*, Cambridge University Press, 2011.

102 A. De Vos, K. Lejaeghere, D. E. P. Vanpoucke, J. J. Joos, P. F. Smet and K. Hemelsoet, *Inorg. Chem.*, 2016, **55**, 2402–2412.